March 27, 2015

Award#: DE-FG02-07ER46356

Project period cover by this final report: August 1 2009 to July 31 2012

Project title: Chemistry and Properties of Complex Intermetallics from Metallic Fluxes

Final report: DOE-Northwestern-ER46356

Program Manager: Dr. Michael Sennett,
Office of Science - Basic Energy Sciences
Department of Energy
Michael.Sennett@science.doe.gov

Principal investigator:
Mercouri G Kanatzidis
Department of Chemistry
2145 Sheridan Road
Northwestern University
Evanston, IL 60208-3113
m-kanatzidis@northwestern.edu

There are no distribution limitations for this report

Executive Summary

This project investigated the reaction chemistry and synthesis of new intermetallic materials with complex compositions and structures using metallic fluxes as solvents. It was found that the metallic fluxes offer several key advantages in facilitating the formation and crystal growth of new materials. The fluxes mostly explored were liquid aluminum, gallium and indium. The main purpose of this project was to exploit the potential of metallic fluxes as high temperature solvent for materials discovery in the broad class of intermetallics. This work opened new paths to compound formation. We discovered many new Si (or Ge)-based compounds with novel structures, bonding and physicochemical properties. We created new insights about the reaction chemistry that is responsible for stabilizing the new materials. We also studied the structural and compositional relationships to understand their properties. We investigated the use of Group-13 metals Al, Ga and In as solvents and have generated a wide variety of new results including several new ternary and quaternary materials with fascinating structures and properties as well as new insights as to how these systems are stabilized in the fluxes. The project focused on reactions of metals from the rare earth element family in combination with transition metals with Si and Ge. For example molten gallium has serves both as a reactive and non-reactive solvent in the preparation and crystallization of intermetallics in the system RE/M/Ga/Ge(Si). Molten indium behaves similarly in that it too is an excellent reaction medium, but it gives compounds that are different from those obtained from gallium. Some of the new phase identified in the aluminide class are complex phases and may be present in many advanced Al-matrix alloys. Such phases play a key role in determining (either beneficially or detrimentally) the mechanical properties of advanced Al-matrix alloys. This project enhanced our basic knowledge of the solid state chemistry and physics of intermetallics, produced new materials with unusual or enhanced properties and ultimately helped improve our understanding of component/matrix interactions that could lead to better Al-matrix alloys.

Accomplishments and project activities

Below we present a report on a number of new syntheses and materials in numbered sections. Each section has subtitles and has its own figure number scheme.

1) Indium flux chemistry

The interesting tendency we identified in this project is that Al flux always produces intermetallics of the type RE/M/Al/Si or RE/M/Al/Ge (where RE is an rare earth element, and M is a transition metal) with incorporation of Al atoms into the crystal structure. For example, it has not been possible in this chemistry to produce ternary silicides of the type RE/T/Si in liquid Al. We found that when excess Ga flux is used quaternary phases form readily in reactions systems involving RE/M/Ga/Ge but not in RE/M/Ga/Si. By switching from Si to Ge and from Ga to In flux we observed parallels in reactivity where it appears to be increasingly more difficult to form quaternary phases in the RE/M/In/Ge system just as in the corresponding Ga/Si systems. In fact, In is often used to re-crystallize ternary germanide phases since it is not incorporated into the final products. For this reason, we investigated whether this tendency was in fact a rule in this chemistry, or whether the scarcity of quaternary indium-containing compounds was attributed to incorrect synthesis conditions. Possible reasons could be inadequate reactions times, too moderate temperatures used, lack of enough systems investigated or even a size effect associated with In. Our investigations of these issues led us to discover that much longer reaction times (several weeks instead of days) in several systems such as RE/Ni/Ge/In could in fact lead to new quaternary phases of indium. Namely, we discovered, $RE_4Ni_2InGe_4$ (RE = Dy, Ho, Er, Tm), the first reported, ordered quaternary intermetallic compounds containing a rare earth, a transition metal, indium and germanium.

The compounds $RE_4Ni_2InGe_4$ crystallize in the monoclinic space group *C*2/*m* with the Mg_5Si_6 structure type. The overall structure is shown in Figure 1(a). Mg_5Si_6 itself as not been synthesized in pure form but it has been identified as an intermetallic phase forming in micron sized islands in an Al matrix of aluminum based alloys, and its structure was elucidated by area selected electron diffraction methods. $RE_4Ni_2InGe_4$ is an ordered quaternary variant of this binary phase. The substructure of $[Ni_2InGe_4]$ is a three-dimensional framework with channels in which rare earth ions are situated. The Ho and Dy analogues exhibit antiferromagnetic ordering at low temperatures. These analogues seem to then undergo a second transition at lower temperature, which is likely due to a spin reorientation. This ordering can be readily disrupted by the application of a magnetic field, resulting in a metamagnetic transitions.

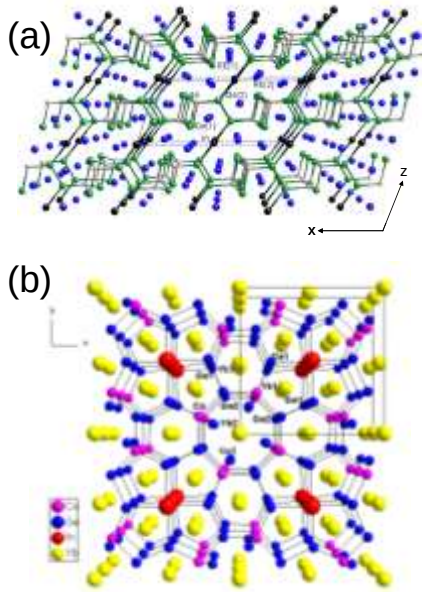

Figure 1. (a) The structure of $RE_4Ni_2InGe_4$. Green atoms are Ge, black atoms In, grey atoms Ni. (b) Structure of $Yb_7Co_4InGe_{12}$.

Corresponding reactions involving Co instead of Ni gave only a small yield (<10%) of the analogous $RE_4Co_2InGe_4$ and high yield of $RE_7Co_4InGe_{12}$ (RE = Dy, Ho, Yb) as thin silver needles. The flux seems necessary to stabilize these compounds because direct combination reactions of the elements and induction heating with various stoichiometric ratios failed so far to form them. $RE_7Co_4InGe_{12}$ crystallizes in the tetragonal *P*4/*m* space group under a new structure type which is characterized by columnar units forming three different types of channels with the RE atoms situated within these channels, Figure 6(b). Investigation of the Yb analog with

magnetic susceptibility measurements, X-Ray Photoelectron Spectroscopy (XPS) and X-Ray Absorption Near Edge Spectroscopy (XANES) revealed that $Yb_7Co_4InGe_{12}$ is a mixed-valent compound, Figure 2. The relative Yb^{3+}/Yb^{2+} ratio is slightly temperature dependent with Yb^{3+} being more populated at higher temperatures. Additionally, resistivity measurements in the presence of an applied field for $Yb_7Co_4InGe_{12}$ (in collaboration with Dr Ulrich Welp at Materials Science Division, Argonne National Laboratory) exhibited negative magnetoresistance at low temperatures (i.e. the resistivity drops with increasing applied field). This behavior is frequently seen in many Kondo or Heavy Fermion systems, and it is attributed to the suppression of scattering of the conduction electrons from the unpaired f-electrons in a high field. Further physicochemical studies of these systems are under way including more detailed magnetic and charge transport properties, heat capacity measurements and Seebeck coefficient measurements.

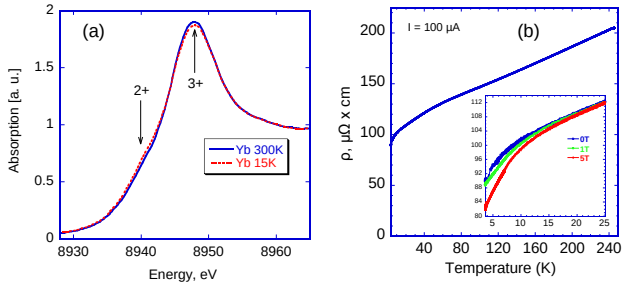

Figure 2. (A) XANES L_{III} absorption edge spectra of Yb in $Yb_7Co_4InGe_{12}$ at 15 K (dashed line) and 300 K (solid line). (B) Variable temperature single-crystal resistivity data for $Yb_7Co_4InGe_{12}$ at zero field. Inset: displays the low temperature resistivity data at 0 T, 1 T and 5 T field. The X-ray absorption near edge spectroscopy (XANES) experiments were performed in Sector 20, bending magnet beamline (PNC/XOR, 20-BM) of the Advanced Photon Source at the Argonne National Laboratory (with Dr Mali Subramanian, APS).

This chemistry also produced the isostructural analog $Yb_7Ni_4InGe_{12}$ which differs from the $Yb_7Co_4InGe_{12}$ by four electrons and suggests the $Yb_7Ni_{4-x}Co_xInGe_{12}$ series should also be stable. In the rigid band approximation this series should allow us to observe how the charge transport and magnetic properties evolve as the Fermi level is adjusted from $0 \leq x \leq 1$ because it is expected to have a large effect on the Yb^{2+}/Yb^{3+} ratio. These systems will be investigated in the near future.

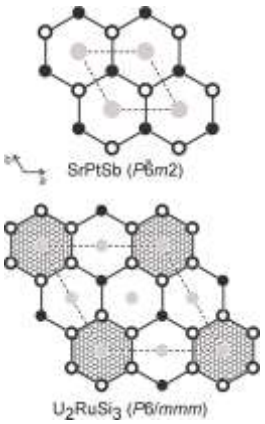

Figure 3. Coloring of honey-comb-like networks for compositions *TX* and TX_3, exemplarily shown for SrPtSb[61] and U_2RuSi_3.[70] Strontium (uranium), transition metal, and antimony (silicon) atoms are drawn as medium gray, black filled, and open circles, respectively. The [PtSb] and [$RuSi_3$] networks are emphasized. The Hückel arene-like $[Si_6]^{10-}$ units in U_2RuSi_3 are shaded.

2) Indium Flux-Growth of Eu_2AuGe_3: A New Germanide with an AlB_2 Superstructure and Low Temperature Phase Transition

During our systematic phase analytical investigations using metal fluxes, we have now investigated the Eu–Au–Ge system using liquid indium as flux medium, in order to overcome the synthetic difficulties of the arc-melting technique (which tends not to give high quality crystals). We studied the structure and properties of the new germanide Eu_2AuGe_3 which we discovered from the reaction of Eu, Au and Ge in an indium metal flux. We observed that Eu_2AuGe_3 undergoes a structural phase transition at 130 K that is accompanied with a change to an orthorhombic space group as well as antiferromagnetic transitions at lower temperatures. Eu_2AuGe_3 crystallizes with a superstructure of the

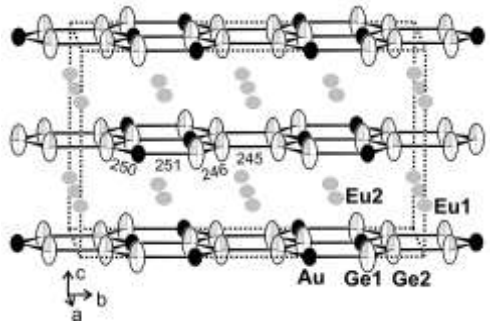

Figure 4. View of the Eu_2AuGe_3 structure approximately along the *a* axis. Europium, gold, and germanium atoms are drawn as medium gray, black filled, and open circles, respectively. The two-dimensional [$AuGe_3$] networks, atom labels, and relevant interatomic distances.

well known AlB_2 family. Within this family of superstructures, two main different coloring schemes of the honey-comb like networks are possible for ternary intermetallic compounds. The two simplest superstructures are presented in Figure 3.

A view of the Eu_2AuGe_3 structure approximately along the *a* axis is presented in Figure 4. As is readily evident from this drawing, the substantial displacements of the two crystallographically independent germanium atoms off the mirror planes (i.e. along the *c*-axis) call for further symmetry reduction at low temperature. Preliminary investigations near liquid nitrogen temperature indeed show superstructure reflections which point to a modulated phase. The unit cell changes to a = 854.25(18) pm, b = 1789.7(3) pm, and c = 854.25(17) pm and β changes to 119.98º. Detailed studies on the low-temperature structural behavior are in progress.

Both europium sites have a slightly distorted hexagonal prismatic coordination, Eu1 with one Au_2Ge_4 and one Ge_6 and Eu2 with two Au_2Ge_4 hexagons. Due to the small distortions within the hexagons, we observe a narrow range for the Eu–Au (335) and Eu–Ge (332–336 pm) distances. The europium atoms have eight europium neighbors at Eu–Eu distances ranging from 429 to 453 pm. In view of the divalency of europium (*vide infra*) and the already shorter Eu–Eu distances of 397 pm in elemental *bcc* europium, Eu–Eu bonding can safely be neglected in Eu_2AuGe_3.

Magnetization. *(a) Single crystals:* The magnetic susceptibility, χ of a single crystal has been measured in two orientations, one being parallel to the applied magnetic field (marked as H ∥ *c*-axis) and other being perpendicular to the field (marked as H ⊥ *c*-axis). In both the measurements, χ increases gradually with increasing temperature and undergoes magnetic ordering (T_N) around 11 K. The χ falls rapidly above 11 K with increasing temperature up to 200 K and above 200 K decreases marginally as if independent of temperature.

The anisotropy between the perpendicular and parallel directions of the single crystal is clearly evident from the inset of Figure 5. Below 11 K, it is seen that the behavior of χ(T) for both directions is slightly different in terms of the value of χ at the lowest temperature. For H ⊥ *c*, χ tends to saturate where as for H ∥ *c* χ tends to increase as T → 0.

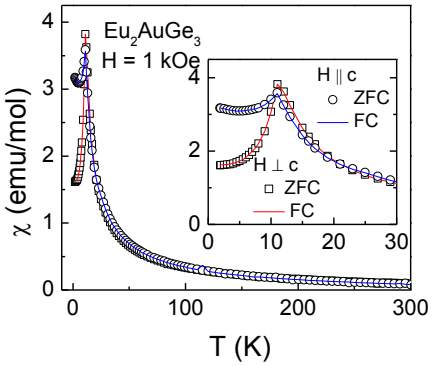

Figure 5. Magnetic susceptibility measured for a single crystal of Eu_2AuGe_3 in two different orientations, magnetic field along the *c*-axis (H ∥ *c*) and magnetic field perpendicular to the *c*-axis (H ⊥ *c*). The measurements were done in both zero field cooled (ZFC) and field cooled (FC) states of the crystal. The ZFC data are shown as open symbols,

where as the FC data is shown as continuous line. The inset shows the low temperature antiferromagnetic peak around 11 K seen in both orientations. The inset also highlights the magnetic anisotropy between the two orientations.

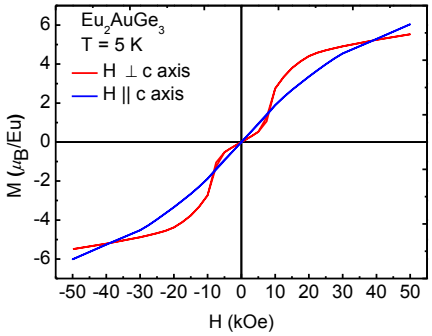

Figure 6. M(H) loops for a single crystal of Eu_2AuGe_3 measured with applied magnetic field perpendicular and parallel to c axis.

Another evidence for the anisotropy between the two crystallographic orientations of Eu_2AuGe_3 can also be seen in from the magnetization as a function of field in the magnetically ordered state, i.e., $T < T_N$. Figure 6 shows the magnetization of the sample while varying the magnetic field with field applied parallel and perpendicular to the *c*-axis of the single crystal. Strong anisotropy effects are observed in Eu_2AuGe_3. In the measurement done with magnetic field perpendicular to *c*-axis ($H \perp c$), the system exhibits metamagnetism around 10 kOe, and tends to saturate at fields above 20 kOe. No hysteresis has been observed. For the $H \parallel c$ measurement, moment increases non-linearly with increasing field, with no trace of saturation till higher fields. Therefore one can attribute the magnetization of this compound to magnetic ions present on the basal plane.

(b) Bulk sample in powder form: The molar magnetic susceptibility of bulk sample of Eu_2AuGe_3 measured in a field of 1 kOe, (Figure 7), also exhibits a sharp peak around 11 K indicating transition to antiferromagnetic state in agreement with the single crystal measurement. Qualitatively, the data of the bulk sample is similar to data measured on single crystal with field perpendicular to the *c*-axis. Below 11 K, in the magnetically ordered state, the system exhibits complex magnetism. Above T_N, the $\chi(T)$ falls rather sharply and decreases with increasing temperature.

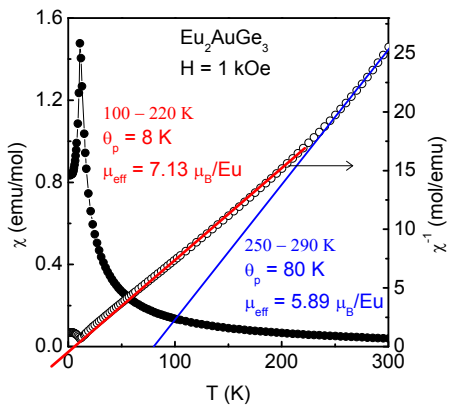

Figure 7. Magnetic susceptibility (χ = M/H) as a function of temperature for Eu_2AuGe_3 (polycrystalline) sample measured in a dc field of 1 kOe. Inverse magnetic susceptibility is also shown in the figure. The blue line passing through the data points is the fit to the Curie-Weiss law.

The plot of inverse susceptibility (χ^{-1}) as a function of temperature deviates from linearity (the Curie-Weiss behavior) below 200 K. Though there is no abrupt anomaly, there is a definite change in slope around this temperature. The fit to the Curie-Weiss law in the temperature range of 250 – 300 K, gives the value of paramagnetic Curie temperature (θ_p) of 80 K and an effective Bohr magnetron number (μ_{eff}) of 5.89 μ_B/Eu ions. As discussed above, the title compound undergoes a structural transition around 130 K, the deviation of $\chi^{-1}(T)$ below 200 K can be taken as an indication of this transition. As there is no corresponding anomaly in $\chi(T)$, the structural transition can be of the second order. The fit to the Curie-Weiss law in the temperature range of 100 – 220 K, gives the value of paramagnetic Curie temperature (θ_p) of 7.5 K and an effective Bohr magnetron number (μ_{eff}) of 7.13 μ_B/Eu ions. The value of μ_{eff} is slightly lower than the expected free ion moment of Eu^{2+} = 7.94 μ_B, and can be attributed to factors

such as crystal field effects.

Specific Heat Data. The specific heat of Eu_2AuGe_3 is shown in Figure 8. The data clearly exhibit a Λ-shaped peak at 11 K, exhibiting long range antiferromagnetic ordering in the system. However, the peak close to 24 K raises an interesting question regarding the origin of such a distinctive Λ-like peak at this temperature. The events responsible for these two peaks in the specific heat are corroborated by corresponding resistivity data presented below. A close inspection of χ(T) (Figure 5) shows that χ rises sharply below 25 K, reminiscent of a ferromagnetic like ordering. This is further evidenced by the positive θ_p values, which indicates ferromagnetic correlations. Therefore, considering the specific heat measurements, the peak at ~24 K could be due to ferromagnetic cluster formation. On further cooling, the system undergoes antiferromagnetic ordering ~11 K, however, as the system is not completely in the antiferromagnetic state, the moment values do not fall to zero as $T \rightarrow 0$.

Within the Debye theory, the low temperature approximation of the measured specific heat is given as $C_p = \gamma T + \beta T^3$ or $C_p/T = \gamma + \beta T^2$ where γ is the contribution from the conduction electrons and β is the lattice contribution.[83] We have fitted the linear region of the C_p/T vs. T plot (T < 11 K), and observed that the electronic (300 mJ/mol K^2) are large and lattice contributions (1 mJ/mol K^4) are small.

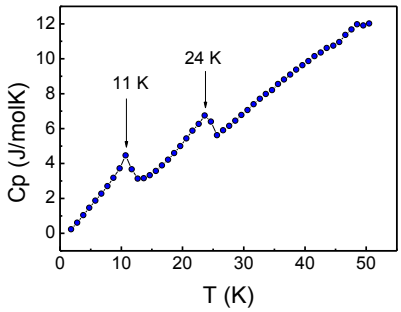

Figure 8. Heat capacity (C_p) for Eu_2AuGe_3 measured as a function of temperature (T) at zero applied fields.

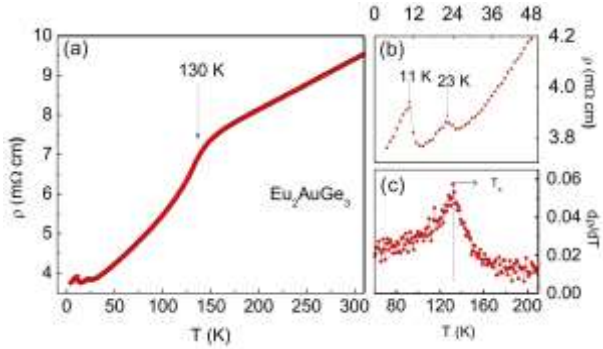

Figure 9. (a) Temperature dependence of the electrical resistivity of Eu_2AuGe_3 with zero applied magnetic field. The arrow shown at 130 K is the structural transformation. (b) Low temperature resistivity data on an expanded scale showing the peaks at 11 and 23 K which correspond to antiferromagnetic ordering and possible ferromagnetic cluster formation, respectively. (c) First derivative of ρ(T). The dotted line exhibits the temperature of structural transition.

Electrical Resistivity. The temperature dependence of the resistivity of single crystal samples of Eu_2AuGe_3 is plotted in Figure 9(a). The resistivity decreases with decreasing temperature which is typical for a metallic conductor. The data also confirms two magnetic orderings in this compound. Figure 9(b) exhibits ρ(T) on an expanded scale, which shows the peaks at 11 K and 23 K respectively in good agreement with the magnetic and heat capacity data. The linear dependence of the resistivity of Eu_2AuGe_3 at temperatures below and above 130 K can be attributed to electron-phonon scattering. This is more clearly seen in the plot of dρ/dT shown in Figure 9(c). In the systems undergoing second order structural

transitions, the effect of spin-fluctuations in the paramagnetic region becomes important, and this can be clearly seen as a peak in the plot of dρ/dT vs. T. Therefore, the anomaly around 130 K in the plot of ρ(T) can be attributed to the change in the crystal structure.

^{151}Eu Mössbauer Spectroscopy. The ^{151}Eu Mössbauer spectra of the Eu_2AuGe_3 sample at 298, 77, and 4.2 K are presented in Figure 10 together with transmission integral fits. At 298 and 77 K, well above the magnetic ordering temperature the spectra could be fitted with a single signal at an isomer shift close to 11 mm/s, indicative for purely divalent europium, in agreement with the susceptibility measurements. The experimental line width is slightly increased with respect to the typical value of ~2.3 mm/s observed for intermetallic compounds. This can be attributed to the two crystallographically independent europium sites which show superposition in the experimental spectrum.

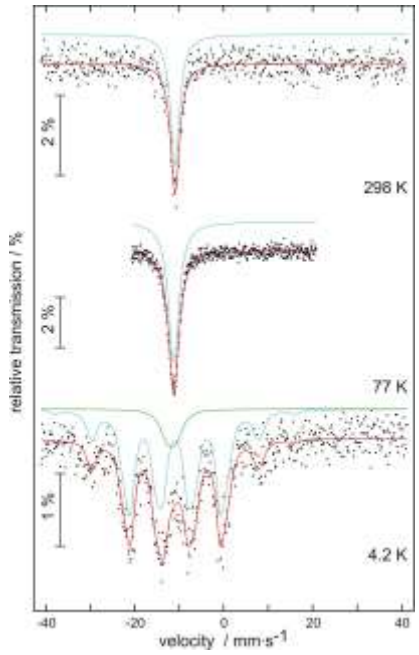

Figure 10. Experimental and simulated ^{151}Eu Mössbauer spectra of Eu_2AuGe_3 at various temperatures.

At 4.2 K, in the magnetically ordered regime we observe magnetic hyperfine field splitting. The spectrum could be well reproduced by a superposition of two spectral components. The main component with 89 % contribution at δ = –10.88(4) mm/s shows a magnetic hyperfine field of 26.0(1) T, typically observed for europium intermetallics. This signal is superimposed by a second contribution with 11 % intensity at δ = –11.7(1) mm/s and a small hyperfine field of only 3.5(8) T. This behaviour can be explained with a domain structure within our sample. The major part of the sample show full magnetic order, while a small degree of the domains shows no magnetic long-range ordering. This can be due to small deviations from the ideal compositions, i. e. domains $Eu_2Au_{1\pm x}Ge_{3\pm x}$. This is likely to occur in such a complex superstructure with eight crystallographically independent europium sites. This may also explain the clustering behaviour discussed above.

The isomer shift in Eu_2AuGe_3 at 77 K (–11.24 mm/s) is slightly smaller than in equiatomic EuAuGe (–10.30 mm/s). This is in agreement with a slightly higher ionicity (smaller *s* electron density) in Eu_2AuGe_3.

Eu_2AuGe_3 is an AlB_2 structure variant which shows temperature dependent polymorphism. The room temperature structure (Ca_2AgSi_3 type) was refined from single crystal diffractometer data. Magnetic susceptibility and ^{151}Eu Mössbauer spectroscopic data show exclusively divalent europium. Eu_2AuGe_3 orders antiferromagnetically at 11 K and shows a metamagnetic transition at 10 kOe. The compound undergoes a structure change below 130 K as determined by X-ray diffraction and supported by resistivity and magnetic susceptibility measurements. Understanding the reasons for the phase transitions will require theoretical electronic structure calculations and the study of nonmagnetic isostructural analogs such as Ca_2AuGe_3. Our experimental work indicates that the isostructural compounds Ca_2AuGe_3 and Sr_2AuGe_3 are also stable.

3) Reactions in Indium flux

Our work with In flux has led to some interesting quaternary phases so far, such as the $RE_4Ni_2InGe_4$ (*RE* = Dy, Ho, Er, Tm) and $RE_7Co_4InGe_{12}$ (*RE* = Dy, Ho, Yb). We have uncovered a rich chemistry revealed by the thorough examination of the ternary *RE*/Au/In system and so we decided to incorporate also a tetrelide such as Ge in order to search for more complex structures and compositions and to compare with the analogous *RE*/*T*/Al/Si or Ge and *RE*/*T*/Ga/Ge or Si systems investigated in this project previously. Among the rare earth compounds, the Yb-based intermetallics which are considered as the hole

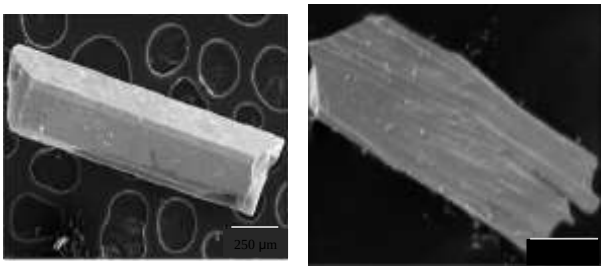

Figure 1. Scanning electron micrograph (SEM) image of (A) a flux-grown $Yb_3AuGe_2In_3$ single crystal and (B) a compact piece of YbAuIn.

counterparts to the isostructural cerium compounds (i.e. f^{13} vs. f^1 systems), have received considerable attention for the past few years. This interest originates from their ability to exhibit various peculiar properties such as intermediate-valence, heavy fermion or Kondo behavior and unusual magnetism. These properties are generally believed to arise from the strong hybridization (interaction) between the localized 4*f* electrons and the delocalized *s*, *p*, *d* conduction electrons.

The new compound $Yb_3AuGe_2In_3$, is particularly interesting and was grown from In flux. It crystallizes as an ordered variant of the YbAuIn structure. We studied the magnetic properties, X-ray Absorption Near Edge Spectroscopy (XANES), electrical resistivity, thermoelectric power and heat capacity measurements are reported. These studies suggest that $Yb_3AuGe_2In_3$ is an intermediate or heterogeneous mixed-valence system. Similar studies are also reported for the parent isostructural YbAuIn in an attempt to investigate the similarities and/or differences between the two compounds.

Crystals of $Yb_3AuGe_2In_3$ grow in indium flux generally as metallic silver rods and in a smaller portion as thinner needles. Figure 1(A) shows SEM image of a typical rod type $Yb_3AuGe_2In_3$ crystal. When other rare earth metals such as Ce, Sm, Eu, Dy and Pr were employed under the same reaction conditions we did not observe analogs of $Yb_3AuGe_2In_3$. In contrast, the *RE*AuIn family of compounds forms with most of the *RE* atoms including Yb.

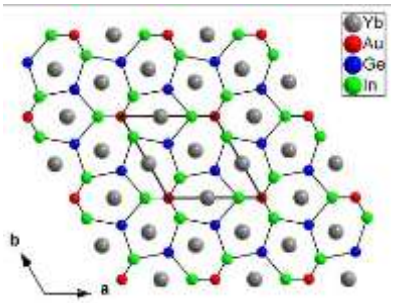

Figure 2. The overall structure of $Yb_3AuGe_2In_3$ as viewed down the *c*-axis. For clarity the bonds to the Yb atoms are not drawn.

Given that YbAuIn and $Yb_3AuGe_2In_3$ are structurally related one would expect that there may be some phase width to $Yb_3AuGe_2In_3$. Although we did not do an exhaustive study of this issue, we have not observed any evidence of solid solution behavior of the type $Yb_3Au_{3-x}Ge_xIn_3$. The lattice parameters as judged by a comparison of powder diffraction patterns from the various batches and the derived lattice parameters from the various samples did not show the type of Bragg line shifts that would be suggestive of this. In addition, we made attempts to synthesize $YbAu_2GeIn_3$ (where only one Ge atom substitutes for Au instead of two, i.e. where x=1 in $Yb_3Au_{3-x}Ge_xIn_3$). The results were negative for the existence of $Yb_3Au_2GeIn_3$ as judged by powder X-ray diffraction. We did not however investigate any compositions which are close to the $Yb_3AuGe_2In_3$. Therefore, we cannot definitely state that $Yb_3AuGe_2In_3$ is a line compound.

Crystal Structure. $Yb_3AuGe_2In_3$ crystallizes as an ordered variant of the YbAuIn structure. YbAuIn contains two crystallographically independent gold sites in trigonal prismatic coordination. The overall structure of the quaternary compound as viewed down the *c*-axis is illustrated in Figure 2. The Au atoms have trigonal prisms formed by the In atoms and those of Ge are built up from ytterbium atoms. Both types of trigonal prisms are capped on the rectangular faces: $[AuIn_6]$ by three ytterbium atoms and $[GeYb_6]$ by three indium atoms, leading to coordination number nine for gold and germanium sites, Figure3. The In atom is eight coordinate, bonded to two other In atoms as well as to two Au, Yb and Ge atoms respectively in an arrangement that could be described as distorted tetragonal prism, Figure 3.
The three-dimensional arrangement that the rare earth atoms adopt in this structure type leads to three exceptional features: i) The *RE* ions within the same layer form triangles so when it comes to antiferromagnetic coupling between nearest neighbors, this topology can cause frustration of the magnetic

interactions. ii) The fact that the magnetic *RE* atoms are stacked in [Yb_3Au] layers that alternate with the non-magnetic [$GeIn_3$] layers, can give rise to indirect exchange interactions. iii) The crystalline electric field surrounding the lanthanide ions frequently induces strong anisotropy, which leads either to Ising or XY spin behavior. Examples of compounds adopting this arrangement are the families of *RE*AuIn and *RE*NiAl. The Au atoms are isolated from one another and are found among the Yb triangles in the net at a Au–Au distance of 7.3153(8) Å, which is equal to the *a*-cell parameter. With respect to the [$GeIn_3$] slab the [Yb_3Au] layer is positioned so that the Yb atoms are aligned with the centers of the pentagons, while the Au atoms are in registry with the In triangles, see Figure 2.

Magnetism. Figure 3(A) shows the temperature dependence of the molar magnetic susceptibility (χ_m) of a ground sample of $Yb_3AuGe_2In_3$ measured from 3 to 400 K with applied field of 500 G. The magnetic susceptibility data follow a modified Curie-Weiss (CW) law that includes a temperature independent component according to the equation $\chi(T) = \chi_0 + C / (T - \theta_p)$. χ_o includes the sum of the temperature-independent contributions, e.g. van Vleck paramagnetism and Pauli paramagnetism (due to conduction electrons). The effective magnetic moment μ_{eff} was deduced from the Curie constant *C*, ($C = \mu_{eff}^2 / 8$). A nonlinear least-squares fit to this equation resulted in $\chi_0 = 3.2 \times 10^{-3}$ emu/mol of Yb atom, Curie - Weiss constant of θ_p = -1.5 K indicating antiferromagnetic interactions and an effective moment of 0.52 μ_B / Yb atom. The inset in Figure 4(A) shows the plot of 1/ ($\chi - \chi_0$) versus temperature. The estimated effective moment of 0.52 μ_B, is only ~ 11.5 % of the value expected for the free-ion Yb^{3+}, 4.54 μ_B. This indicates that the compound contains both Yb^{2+} and Yb^{3+} species. In order to confirm the presence of Yb^{3+} species in the title compound we performed XANES studies that are discussed below.

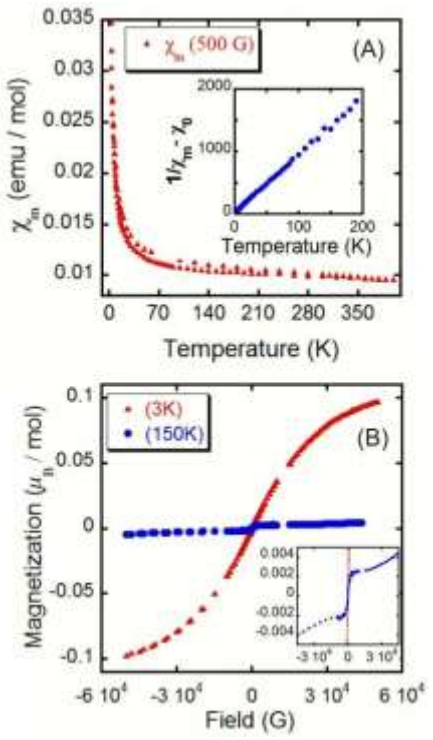

Figure 3. (A) Temperature dependence of the molar susceptibility χ_m of $Yb_3AuGe_2In_3$ (ground samples) with an applied field of 500 G. The inset shows the plot of 1/ ($\chi_m - \chi_0$) versus temperature. (B) Magnetization data of $Yb_3AuGe_2In_3$ collected at 3 and 150K.

The field dependence of the magnetization *M*(*H*) for a ground sample of $Yb_3AuGe_2In_3$ at 3 and 150 K are shown in Figure 3(B). The data at 3 K exhibit linear behavior up to about 12 kG at which point the slope changes continuously until ~33 kG and then it becomes linear again but with a much shallower slope. No signs of saturation up to the highest attainable field of 50 kG were observed. The magnetization curve taken at 150 K showed a very different picture. There is a strong field dependent response up to ~ 1.2 kG, which saturates at ~ 11 kG, while above that field *M*(*H*) it becomes linear up to the highest obtainable field. This suggests that, there is probably a small ferromagnetic component in the $Yb_3AuGe_2In_3$ sample which may be part of the structure itself, however, we cannot rule out the fact that it may also be an extrinsic impurity.

XANES. To further probe the Yb valence state in $Yb_3AuGe_2In_3$ and YbAuIn, we performed X-ray absorption measurements at the Yb L_{III}-edge. The near-edge spectra for both compounds obtained at temperatures of ~15 - 18 K and 300 K and at ambient pressure showed no significant difference between the two temperatures, suggesting that the Yb valence remained stable in the measured temperature range. The spectra at 295 and 300 K (room temperature) for $Yb_3AuGe_2In_3$ and YbAuIn, respectively, are given in Figure 4(A). The main absorption peak (white line resonance) of the spectrum for both spectra is centered at ~8941.5 eV, which is attributed to divalent Yb atoms.

The spectra also revealed the presence of a weaker feature (shoulder) at ~8949.5 eV, indicating that some trivalent Yb is also present. Since in both compounds under study there is only one unique crystallographic Yb site (as determined by the time scale of diffraction), there could be two plausible scenarios; one in which $Yb_3AuGe_2In_3$ and YbAuIn could be classified as an intermediate valence compounds with all Yb atoms having a non-integer valence, and a second where the materials are heterogeneous mixed-valence compound, in which the Yb atoms alternate between 2+ and 3+ state in various domains.

The relative amounts of the two electronic configurations were determined by decomposing the normalized Yb XANES into a pair of arc-tangents (representing the edge step) and Lorentzians functions (representing the white line resonance). Fitting of the data with the above technique for $Yb_3AuGe_2In_3$, resulted in ~ 85.2% of Yb^{2+} and ~ 14.8% of Yb^{3+} which leads to an average Yb valence of ~ 2.15. For YbAuIn, similar analysis led to an average Yb valence of ~ 2.22. This is in agreement with the magnetic susceptibility data for this compound discussed above. In the case of YbAuIn however, while majority of the Yb is present in the intermediate state, a careful inspection and analysis of the EXAFS indicates that

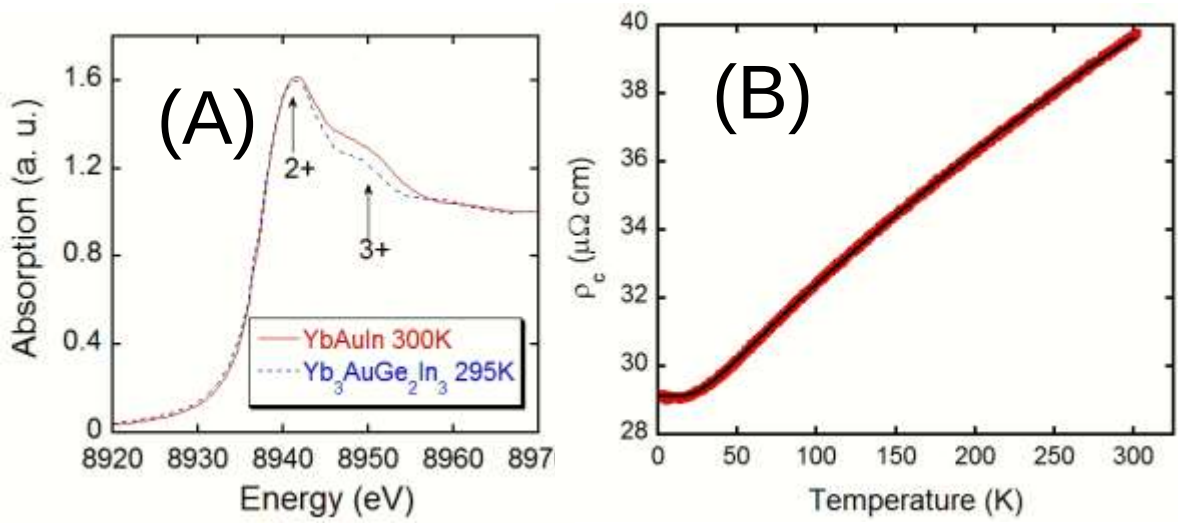

Figure 4. (A) First derivative L_{III} absorption edge spectra of Yb in $Yb_3AuGe_2In_3$ at 295 K (dashed line) and in YbAuIn at 300 K (solid line). (B) Temperature variation of the electrical resistivity $\rho(T)$ of $Yb_3AuGe_2In_3$ from 2.48 to 302.3 K. The dashed line is a fit of the experimental data (squares) to the Bloch – Grüneisen – Mott formula (2).

the sample might also contain ~ 3 - 5% of a trivalent oxide impurity component. Taking into account the possible presence of an oxide component we determine the intrinsic valence of Yb in YbAuIn to be ~ 2.17. We estimate the uncertainty in the absolute valence to be ~ 5%, arising mainly from correlations between parameters used to represent the edge-step and white line resonances. The Yb^{3+} fraction for $Yb_3AuGe_2In_3$ is consistent with that estimated independently from the magnetic measurements described above.

Resistivity. The $Yb_3AuGe_2In_3$ compound is clearly metallic. The temperature variation of the electrical resistivity $\rho(T)$ of $Yb_3AuGe_2In_3$ between 2.48 and 302.3 K is presented in Figure 4(B). The resistivity data measured on single crystals along the *c*-axis and at zero applied field reveal metallic conductivity with a room temperature resistivity value ρ(300K) of 39.6 $\mu\Omega$ cm. When a magnetic field of 6 Tesla was applied the compound showed no magnetoresistance. In the measured temperature range, the resistivity of $Yb_3AuGe_2In_3$ can be well described by the Bloch – Grüneisen – Mott (BGM) formula:

$$\rho(T) = \rho_0 + 4R\Theta_D\left(\frac{T}{\Theta_D}\right)^5 \int_0^{\frac{\Theta_D}{T}} \frac{x^5\,dx}{(e^x - 1)(1 - e^{-x})} - KT^3 \qquad (1)$$

where ρ_0 is the residual resistivity, the second term represents electron-phonon scattering, and the third term accounts for Mott's *s-d* interband electron scattering. The least-squares fitting procedure of (1) yielded the parameters ρ_0 = 29 $\mu\Omega$ cm and a Debye temperature Θ_D = 166 K, which is in good agreement with the Θ_D value that was estimated from the specific heat results (see below). The relatively low Θ_D is consistent with the presence of heavy atoms in the structure and suggests a soft lattice.

Heat Capacity . The temperature dependent specific heat from 1.8 to 50 K for $Yb_3AuGe_2In_3$ is shown in Figure 5(A). The data can be described well by a Debye function (2) where the first and second term correspond to the electronic and the phonon contribution, respectively. *N* is the number of the atoms in the formula unit and $x = \hbar\omega/k_BT$.

$$C_p(T) = \gamma T + 9NR\left(\frac{T}{\Theta_D}\right)^3 \int_0^{\frac{\Theta_D}{T}} \frac{x^4\,dx}{(e^x - 1)^2} - KT^3 \qquad (2$$

A fit to the experimental points resulted in a Debye temperature Θ_D of about 178 K, and an electronic specific heat coefficient $\gamma \approx 31$ mJ / mol K^2, which was determined from γ (= C_p / $T)_{T\to 0}$ at low temperatures. The observed Θ_D value is slightly higher than the value obtained from the resistivity measurements (166 K).Therefore the compound does not appear to be a heavy-fermion material according to the arbitrary classification of these compounds into "light", "moderate" and classical heavy-fermions with γ values lying in the range of ~ 50-60, 100-400 and > 400 mJ / mol K^2 respectively. Nevertheless, this value of electronic specific heat compares well with the ones found in other mixed valent or intermediate compounds such as the $YbAl_2$, $YbAl_3$, $YbMgCu_4$, $YbNi_4Si$, and $YbInAu_2$ in which γ ranges at 15 – 62 mJ / mol K^2.

The temperature dependent specific heat data measured at a temperature range of 1.8 to 50 K for YbAuIn are shown in Figure 5(B). The data can also be described well by the Debye function (2). A least-square fit to the experimental points resulted in a Debye temperature Θ_D of about 156 K, and an electronic specific heat coefficient $\gamma \approx 84$ mJ/mol K^2, which was determined from γ (= $C_p/T)_{T\to 0}$ at low temperatures. According to the arbitrary classification of the heavy-fermion compounds mentioned above, YbAuIn could be classified as a "light" heavy-fermion compound.

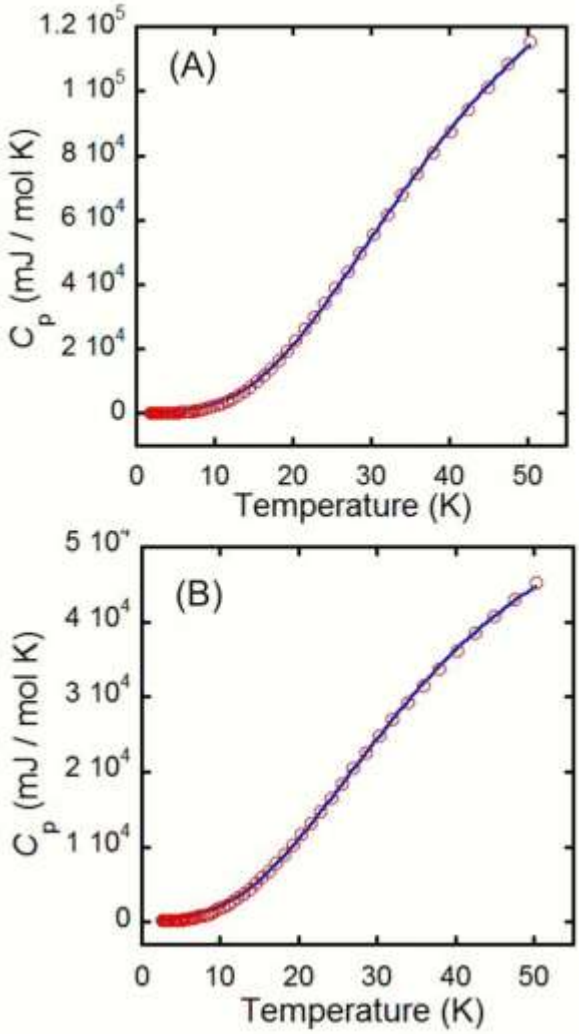

Figure 5. Heat capacity (C_p) of $Yb_3AuGe_2In_3$ (A) and YbAuIn (B) measured from 1.8 to 50.3K. The experimental data (circles) are fitted with Debye formula (2) (solid line).

4) The compound: $Yb_5Ni_4Ge_{10}$

Along a different line of inquiry, we discovered the new compound $Yb_5Ni_4Ge_{10}$ which was obtained as single crystals and in high yield from reactions run in liquid indium. Single crystal X-ray diffraction data showed that it crystallizes in $Sc_5Co_4Si_{10}$ structure type in the tetragonal space group *P*4/*mbm*. $Yb_5Ni_4Ge_{10}$ was obtained from Yb/Ni/Ge reactions in liquid In, from which the new tetragonal phase was isolated in high yield (>95 %). The light gray rod-shaped single crystals up to 5 mm in length were stable in air and no decomposition was observed even after several months. SEM images of typical rod-like crystals of $Yb_5Ni_4Ge_{10}$ as grown from the flux synthesis are shown in Figure 1. Other synthetic techniques such as arc melting, high frequency induction heating, direct heating in resistive furnaces were not successful in producing the title compound. The structure is a three-dimensional framework of $[Ni_4Ge_{10}]$ atoms with voids filled by Yb atoms, Figure 1. The Ni and Ge atoms form pentagons, hexagons and octagons along the *ab* one dimensional plane which are inter-connected along *c*-axis via Ni-Ge-Ni zigzag chains. Magnetic measurements on $Yb_5Ni_4Ge_{10}$ crystals show paramagnetic behavior with a lack of long range magnetic ordering down to 2 K. The magnetic susceptibility deviates from the Curie-Weiss law below 100 K, presumably due to crystal field effects from Yb^{3+} ions. In specific heat measurements the compound exhibits non-Fermi liquid-like behavior at low temperatures.

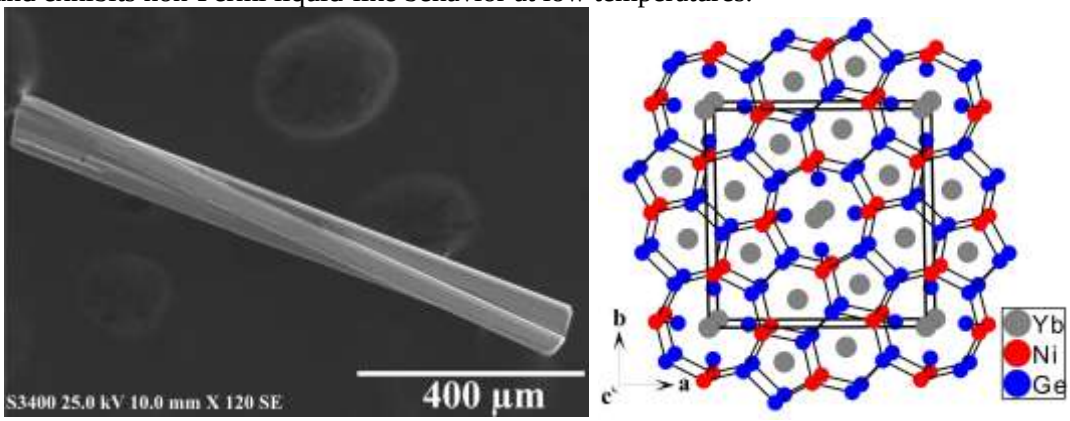

Figure 1. Left: SEM image of two overlapping typical single crystals of $Yb_5Ni_4Ge_{10}$. Right: The structure of $Yb_5Ni_4Ge_{10}$ as viewed along the *c*-axis with the unit cell outlined

5) Metallic Yb_2AuGe_3: An ordered Superstructure in the AlB_2 type Family with Mixed Valent Yb and a High Temperature Phase Transition

RE_2TX_3 intermetallics (X=group 14 element) can be derived from the prototype AlB_2 structure by Bärnighausen formalism applying three different types of symmetry operations like klassengleiche (k), translationengleiche (t) and isomorphic transitions (i). Many of these phases, such as RE_2PdSi_3 (*RE* = Gd, Tb, Dy, Ho) crystallize in hexagonal structures or in its more or less ordered derivatives as for example Eu_2AuGe_3 which crystallizes in orthorhombic superstructure in *Fmmm* space group. In RE_2TX_3, the *RE* atoms occupy the aluminum position, while the *T* and *X* atoms form the two-dimensional infinite network.

The ability to obtain large single crystal specimens from the metal flux technique used in this DOE funded project is contributing a great deal to our understanding of the detailed structures of these compounds. Assignment of space group to Er_2RhSi_3 is a classic example on this context. X-ray diffraction data on powder samples suggested a non-centrosymmetric space group (*P*62*c*) for Er_2RhSi_3, but later single crystal X-ray diffraction (XRD) studies confirmed the centrosymmetric space group $P6_3/mmc$ which also corresponds to the hexagonal crystal system.

We targeted the synthesis of single crystal Yb_2AuGe_3 using indium as the metal flux because relatively few germanides exist in the RE_2TX_3 series. This is the first ytterbium based compound within the RE_2TX_3

family that crystallizes in the ordered superstructure of AlB_2 structure type. Among the rare earths, the Yb-containing compounds have particular scientific interest because they can exhibit two energetically similar electronic configurations: the magnetic Yb^{3+} ($4f^{13}$) and the nonmagnetic Yb^{2+} ($4f^{14}$) one. In this case, the roles of the 4*f* electron and 4*f* hole can be interchanged, and many phenomena, such as intermediate valence, Kondo effect or heavy-fermion behavior and even structural transformation. Yb_2AuGe_3 shows a phase transition at higher temperature as observed in temperature dependent powder XRD studies. We performed magnetic measurements which suggested that Yb_2AuGe_3 has Yb atoms in a mixed valent state and the material is metallic while temperature dependent electrical resistivity measurements at low temperature indicate possible Fermi-liquid behavior. We also obtained heat capacity data which also suggest moderate heavy fermion behavior for Yb_2AuGe_3.

Crystal Structure

Yb_2AuGe_3 crystallizes in the Ca_2AgSi_3 type structure which is an ordered superstructure of AlB_2 family (Table 1). This is the first example of Yb based germanide in the RE_2TX_3 family that crystallizes in an ordered superstructure of AlB_2. In Yb_2AuGe_3, *M*1, *M*2 and *M*3 atoms form hexagons that form graphite-like layers (Figure 2). The shortest distance between the hexagonal layers is 4.2498(8) Å for Yb_2AuGe_3. The Yb atoms are intercalated between the [M_6] layers. The layers are stacked along the *b*-axis in an eclipsed fashion as shown in Figure 3. The short *M*1-*M*2 distance is a hint of puckering of M_6 layer, but slightly large atomic displacement parameters of *M*3 along the *b*-axis suggests a certain amount of disorder in the stacking registry of the [M_6] layers. We hypothesized that this disorder could induce a temperature dependent phase transition in Yb_2AuGe_3 at ~130 K from orthorhombic to a monoclinic system. However, the low temperature single crystal data analysis for Yb_2AuGe_3 down to 4 K did not show any hint of phase transformation and we did not observe anomalies in electrical resistivity data in the temperature range 2-300 K (shown in physical property section below).

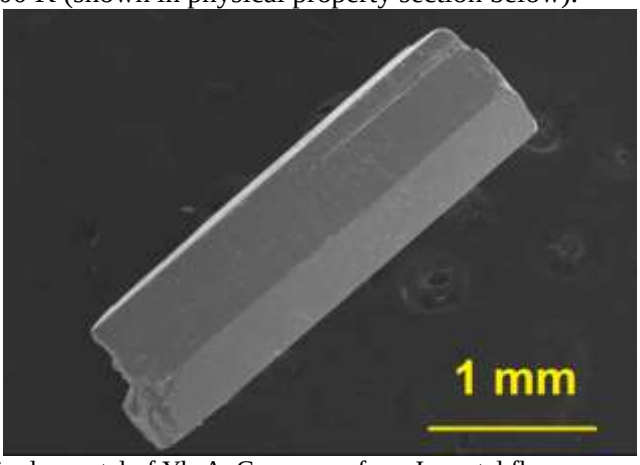

Figure 1. SEM image of a single crystal of Yb_2AuGe_3 grown from In metal flux.

A phase transition was found at high temperature as observed in the powder XRD data from 303-1073 K, (Figure 4). Above 873 K, Bragg peaks corresponding to the superstructure reflections progressively decreased in intensity and peaks which correspond to the substructure (hexagonal) increased. In order to simulate the powder pattern we removed the superstructure reflections from the single crystal XRD data and refined the substructure of Yb_2AuGe_3, in the AlB_2, *P*6/*mmm* space group and lattice constants are $a = b = 4.2476$ (6) Å, $c = 4.2376(8)$ Å. The simulated powder pattern obtained is in agreement with the experimental powder diffraction pattern obtained at or above 873 K.

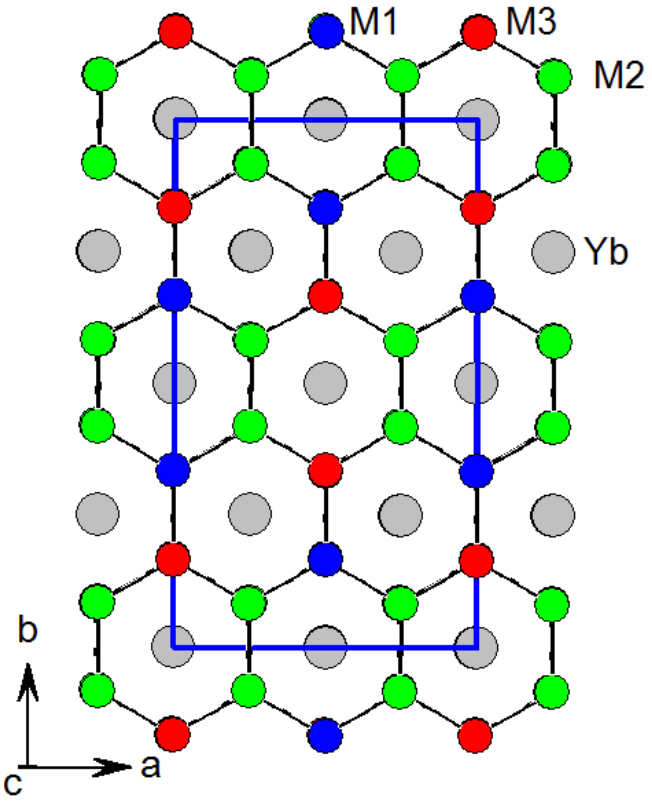

Figure 2. View of the Yb_2AuGe_3 structure approximately along the *b* axis; M1 = Au1+Ge1, M2 = Au2+Ge2 and M3 = Au3+Ge3. Ytterbium atoms are embedded in the two-dimensional hexagonal [$AuGe_3$] networks.

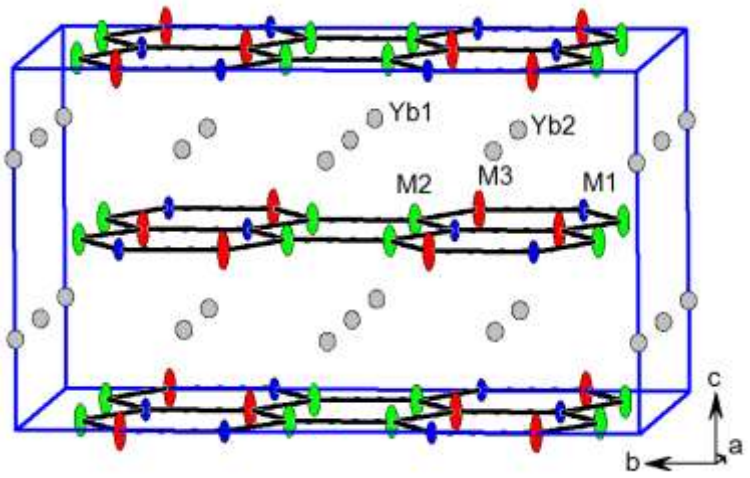

Figure 3. View of the Yb_2AuGe_3 structure approximately along the *a*-axis; M1 = Au1+Ge1, M2 = Au2+Ge2 and M3 = Au3+Ge3.

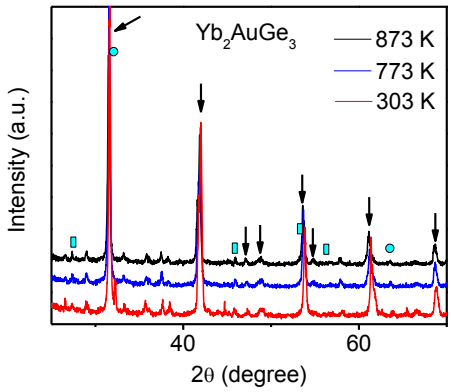

Figure 4. Comparison of powder XRD patterns of Yb_2AuGe_3 at 303 K, 773 K and 873 K. The peaks which originate from the substructure (hexagonal structure) of the compound are shown by arrows. The unreacted Ge (cubic, $Fd\bar{3}m$ space group) and In (tetragonal, *I*4/*mmm* space group) peaks are shown by rectangular and circular mark-ups, respectively. The remaining peaks correspond to superstructure diffractions.

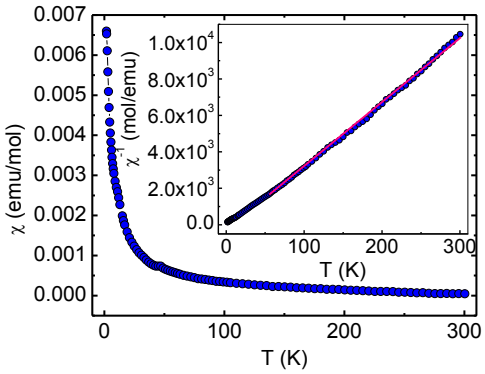

Figure 5. Magnetic susceptibility (χ = M/H) as a function of temperature for Yb_2AuGe_3 (polycrystalline) sample measured in a dc field of 1 kOe. The inset highlights the Inverse magnetic susceptibility (χ^{-1} = H/M).

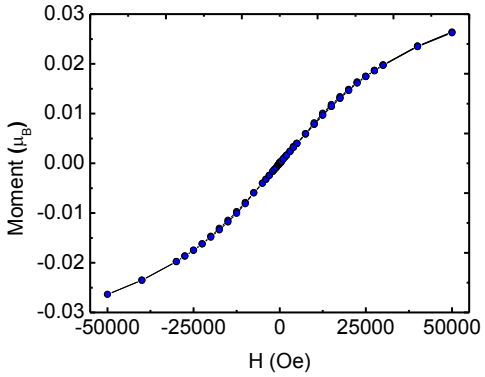

Figure 6. Magnetization as a function of applied magnetic field at 5 K for a polycrystalline sample of Yb_2AuGe_3.

Magnetic Measurements. Figure 5 shows the temperature dependence of the molar magnetic susceptibility (χ_m) of a ground sample of Yb_2AuGe_3 measured from 3 to 300 K with applied magnetic field of 1000 Oe. No long-range magnetic order could be observed down to 3 K; however there is an upturn in the magnetic susceptibility data around 50 K suggesting paramagnetic behavior. From the linear region of the inverse susceptibility plot (50-300 K), the calculated value for paramagnetic Curie-Weiss

temperature (θ_p) is 10.9 (1) K suggest weak ferromagnetic coupling between the Yb moments. The estimated effective moment of 0.33 (2) μ_B, is only ~ 7 % of the value expected for the free-ion Yb^{3+}, 4.54 μ_B. This indicates that the compound contains both Yb^{2+} and Yb^{3+} moieties. The field dependence of the magnetization $M(H)$ for Yb_2AuGe_3 ground sample at 5 K can be found in Figure 6 exhibit linear behavior up to about 24 kG at which point the slope changes continuously until about 50 kG, but no signs of saturation up to highest attainable field of 50 kG were observed.

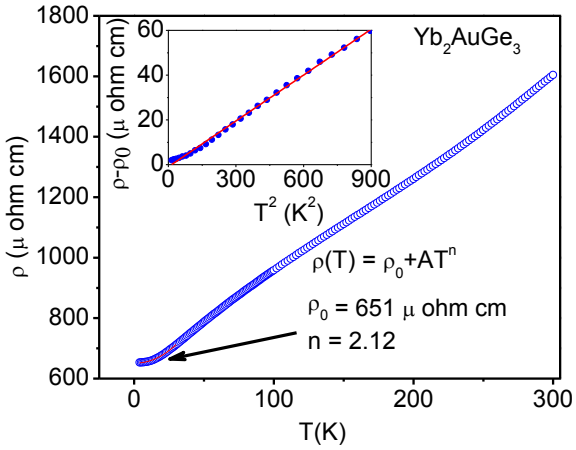

Figure 7. Temperature dependent electrical resistivity $\rho(T)$ of a single crystal sample of Yb_2AuGe_3 in the temperature range 2-300 K. The low temperature data has been fitted to the power law, $\rho = \rho 0 + AT^n$. The values obtained from the fit are shown in the figure. A plot of ρ-ρ_0 vs. T^2 showing a linear relationship is shown as an inset.

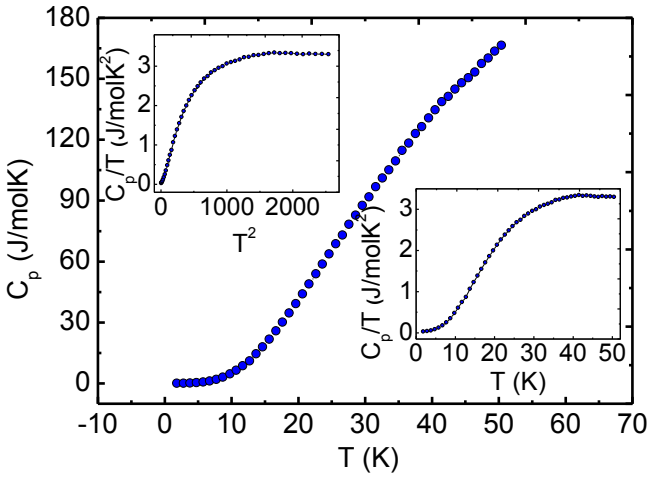

Figure 8. Heat capacity (C_p) of Yb_2AuGe_3 measured from 1.8-50 K. The inset figures are C_p/T Vs. T and C_p/T Vs. T^2.

Resistivity. The temperature dependent electrical resistivity $\rho(T)$ of Yb_2AuGe_3 in the range 2-300 K is presented in Figure 7. The resistivity data measured on single crystals along the *c*-axis and at zero applied field reveal metallic conductivity with a room temperature resistivity value ρ(300K) of 1600 $\mu\Omega$ cm. This value of room temperature resistivity, ρ(300) for Yb_2AuGe_3 was comparable with the previously reported Eu_2AuGe_3 (947 $\mu\Omega$ cm).To further investigate the correlative nature of the conduction electrons in the

compound, we fitted the $\rho(T)$ vs. T curve with the power-law function $\rho(T) = \rho_0 + AT^n$ where, $\rho(T)$ is resistivity at any temperature T, ρ_0 is residual resistivity, A and T are fitting parameters in the low temperature range (2-30 K).[71] According to the Fermi-liquid theory, at low temperatures, the resistivity varies as $\rho = \rho_0 + AT^2$. Experimentally it has been observed that when electron-electron scattering dominates over electron-phonon scattering, $\rho \propto T^2$. The non-linear fitting of the curve in this temperature range gave ρ_0 value of 651 μohm cm and $n = 2.12$. Thus, in the prescribed temperature range the power law is reduced to $\rho(T) = \rho_0 + AT^2$ which is consistent with the Fermi-liquid behavior. To better illustrate the Fermi-liquid behavior in Yb_2AuGe_3, the resistivity data plotted as $[\rho(T) - \rho_0]$ vs. T^2 as an inset in Figure 7. The linearity of the data proves that the compound Yb_2AuGe_3 has a strongly correlated Fermi-liquid ground state at low temperature. In this context, it worthwhile to mention that the compound CeRuSi, a "moderate heavy fermion" with a γ value of 180 mJ/molK^2 also shows Fermi-liquid behavior.[76] The resistivity varies linearly with T^2.

Heat Capacity. The temperature dependent specific heat from 1.8-50 K for Yb_2AuGe_3 is shown in Figure 8. The absence of long-range magnetic ordering in Yb_2AuGe_3 was already observed from the magnetic susceptibility measurements. Further evidence for the same can be found in the plot of specific heat Vs temperature. The C_p decreases as the temperature is lowered. The $C_p(T)$ does not exhibit any anomaly, thus ruling out any type of long range phase transitions. C_p(T) has been shown in different forms as insets in the Figure 8. The observed specific heat at low temperatures can be described by the equation: $C_p = \gamma T + \beta T^3$, which describes that the total specific heat of the sample comprises of the contributions from the electronic part (coefficient of electronic specific heat, γ) as well as the lattice part (β). Thus, at low temperatures C_p should vary as a function of T^3, which is the plot of C_p/T vs. T^2 should be a straight line. Such a plot is convenient for calculating the values of both γ and β.

A fit from the plot of C_p/T vs. T^2 (T = 7-15 K), resulted the value of γ = 109 mJ/mol K^2 suggesting a moderate heavy-fermion material according to the arbitrary classification of these compounds into "light", "moderate" and classical heavy-fermions with γ values lying in the range of ~ 50-60, 100-400 and > 400 mJ / mol K^2 respectively. This value of electronic specific heat compares well with the ones found in other mixed valent or intermediate compounds such as $YbNi_2Ge_2$, $YbRh_2Si_2$ and $Yb_2Co_3Ga_9$. Debye temperature, Θ_D calculated using the following equation resulted 157 K, normal for Yb based intermetallics. The Debye temperature is a fundamental constant of a solid and is a measure of phonon contribution toward the overall heat capacity and a low value of Θ_D indicates a low total heat capacity at low temperatures. Generally materials with heavy atoms exhibit low Debye temperatures.

Table 1. Crystal data and structure refinement for Yb_2AuGe_3 at 293(2) K.

Empirical formula	Yb_2AuGe_3
Formula weight	764.39
Temperature	293(2) K
Wavelength	0.71073 Å
Crystal system	Orthorhombic
Space group	*Fmmm*
Unit cell dimensions	a = 8.5124(17) Å, α = 90.00° b = 14.730(3) Å, β = 90.00° c = 8.4995(17) Å, γ = 90.00°
Volume	1065.7(4) Å^3
Z	8

Density (calculated)	9.528 g/cm^3
Absorption coefficient	79.326 mm^{-1}
F(000)	2531
Crystal size	0.12 x 0.10 x 0.08 mm^3
θ range for data collection	4.79 to 34.26°
Index ranges	-11<=h<=13, -23<=k<=23, -12<=l<=13
Reflections collected	3715
Independent reflections	640 [R_{int} = 0.0982]
Completeness to θ = 34.26°	98.5%
Refinement method	Full-matrix least-squares on F^2
Data / restraints / parameters	640 / 0 / 26
Goodness-of-fit	1.188
Final R indices [>2σ(I)]	R_{obs} = 0.0544, wR_{obs} = 0.1201
R indices [all data]	R_{all} = 0.0567, wR_{all} = 0.1212
Extinction coefficient	0.00019(4)
Largest diff. peak and hole	8.003 and -11.322 e·Å^{-3}

$R = \Sigma||F_o|-|F_c|| / \Sigma|F_o|$, $wR = \{\Sigma[w(|F_o|^2 - |F_c|^2)^2] / \Sigma[w(|F_o|^4)]\}^{1/2}$ and calc $w=1/[\sigma^2(Fo^2)+(0.0306P)^2+142.9431P]$ where $P=(Fo^2+2Fc^2)/3$

6) Structure and Unusual Magnetic Properties of $YbMn_{0.17}Si_{1.88}$

In general, rare earth ions in the intermetallic compounds exist in the trivalent state. However, because of the greater stability of the empty, half-filled or filled 4f shells, the Ce, Eu, and Yb ions may also exist in other valence states, resulting in compounds with unusual physical and magnetic properties. Among them, ytterbium-based compounds are of considerable interest because they can show a wide variety of properties such as Kondo effects. These properties are associated with the unstable 4*f* shell, which can develop two electronic configurations, a completely filled, non-magnetic divalent (Yb^{2+}) and one electron deficient, magnetic trivalent (Yb^{3+}). A competition between these two states often creates mixed and/or intermediate valent Yb and this fact is the motivation behind the study of the Yb-Mn-Si system we report here. .

Following our previous investigation of anomalous thermal expansion in the square net $Yb_4T_xGe_8$ (*T* = Cr-Ni, Ag) compounds[1] and considering the fact that only $YbNiSi_2$ in the $CeNiSi_2$ type structure[19] has been reported, we focused our studies on the synthesis of Mn analogs via reactions in liquid indium. These reactions led to single crystals of $YbMn_{0.17}Si_{1.88}$ the structure of which was refined using X-ray single crystal data. $YbMn_{0.17}Si_{1.88}$ crystallizes in the rare monoclinic polar space group $P2_1$, which is an ordered structure of the compound reported by Norlidah et al.[2] Magnetic susceptibility studies on selected single crystals of $YbMn_{0.17}Si_{1.88}$ show that it is an intermediate/mixed Yb valent compound exhibiting a magnetic transition associated with valence change. This unusual magnetic behavior is also reflected in the specific heat measurements.

Reaction chemistry

Carrying out reactions between Yb, T and Si in liquid indium favors the formation of YbT_2Si_2 as the main compound and a few single crystals of AlB_2 - type $YbSi_2$ as a side product. Our recent investigations in

the Yb/T/Si system in indium flux produced the compounds YbT_xSi_{2-x} (T = Cr, Fe, Co) which crystallize in the $ThSi_2$ structure type. However, no Mn analogues were obtained under the same reaction conditions. Only when an excess of Mn was used did we obtain plate shaped grey colored crystals of $YbMn_{0.17}Si_{1.88}$. Powder XRD confirmed that this phase did not crystallize in the $ThSi_2$ structure type. Mn_3Si was the main impurity observed in this reaction in addition to some unreacted silicon. $YbMn_{0.17}Si_{1.88}$ single crystals have metallic luster and are stable in air for months. In order to suppress the main impurity of Mn_3Si attempts were made using Sn and Ga as fluxes. Neither of these alternative fluxes succeeded in producing the corresponding YbT_xSi_{2-x} compounds.

Crystal structure

$YbMn_{0.17}Si_{1.88}$ crystallizes in the monoclinic system, Table 1 in this section. The average structure is shown in Figure 1B, and is closely related to the previously reported disordered orthorhombic structure (Figure 1A). The structure can be described as the stacking of three AlB_2 and one $BaAl_4$ slabs along the [010] direction with the Yb atoms residing within the channels formed by the connection of the two layers. Alternatively, the structure can also be described as Mn and Si atoms (excluding Yb atoms) located in alternating layers stacked along the long *c*-axis in the sequence: Mn-Si1-Si2-Si4-Si4-Si2-Si1-Mn. The bonds to the Yb atoms are omitted in the figure to emphasize the three-dimensional (3D) Mn/Si framework and its channels. The $BaAl_4$ slab is formed by partially filled manganese sites and fully occupied Si3 sites, while the AlB_2 slabs are formed by ytterbium and three Si atoms. Mn and Si3 atoms in the $BaAl_4$ slab are arranged as distorted square nets (Figure 1C). In this the tetrahedrally coordinated (4 Mn atoms) Si3 atoms form a 2-dimensional square net that extends in the *ac*-plane and is capped by Mn atoms alternatively above and below this plane forming an overall puckered layer. The AlB_2 layers on the other hand are composed of two different types of Si zigzag chains (Figure 1D). The layer containing Si4 atoms is less puckered (Si4-Si4-Si4 bond angle is 136.7˚) compared to the layer containing Si2 and Si1 atoms (Si2-Si1-Si2 bond angle is 107.2˚). These layers are connected along the c-axis forming Si_6 hexagons and connected in a slightly distorted fashion (Figure 2) adopting an overall monoclinic system.

Structural refinement in the monoclinic system improved the bond distances compared to the refinement in the previously reported orthorhombic system.[2] The shortest Si-Si distance is2.0467 Å is much shorter than the typical Si-Si covalent bond length of 2.34 Å, but such short distances have reported in $Yb_2Fe_4Si_9$ (2.07 Å)[48] and in the Zintl phase $CaSi_2$ (2.11 Å) at 360 kbar.[3] The 3*d* electrons of Mn and 4*f* electrons likely contribute to the Mn-Yb2 bond and this electron transfer seems to create the mixed valence at the Yb sites ($Yb^{(2+\delta)}$). As a result the Mn-Si2 distances are very short (2.0298 Å) in the square net.

The coordination environments of the two Yb atoms are shown in Figure 3. Both sites have high coordination numbers (*CN*) as is usual for such intermetallic compounds: *CN* 20 for Yb1 with 12 Si + 8 Yb for Yb1 and *CN* 21 for Yb2 with 10 Si + 5 Mn + 6 Yb for Yb2. Although the coordination numbers of both ytterbium sites are similar, there are negligible differences in the interatomic distances. The twelve nearest silicon neighbors of Yb1 site has Yb-Si distances ranging from 2.91 Å to 3.25 Å and Yb2 has closest Si neighbors within the range of 2.88 Å to 3.01 Å. These contacts are most likely bonding. It is also interesting to mention Yb2 has no closest Mn atom compared to 5 Mn atoms in the case of Yb1. The average Yb-Si and Yb-Yb distances for Yb1 and Yb2are 2.983 Å and 3.873 Å and 2.951 Å and 3.857 Å respectively. These suggest no significant differences between ytterbium sites. The average Yb-Mn distance obtained for Yb2 is 3.126 Å, which is longer than the average Yb-Si distance and consistent with the larger size of Mn atom compared to Si.

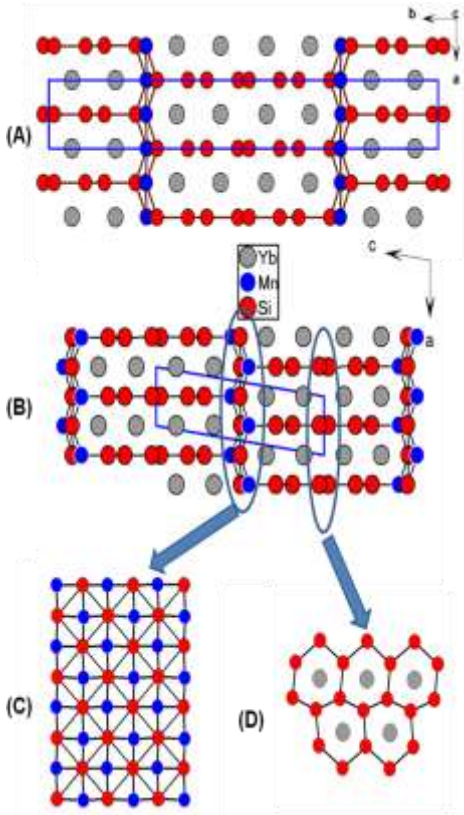

Figure 1. (A) Crystal structure of $YbMn_{0.17}Si_{1.88}$ in the orthorhombic system projected along [001] (B) Crystal structure of $YbMn_{0.17}Si_{1.88}$ in the monoclinic system projected along [010], (C) $BaAl_4$ type layer (D) AlB_2 layer

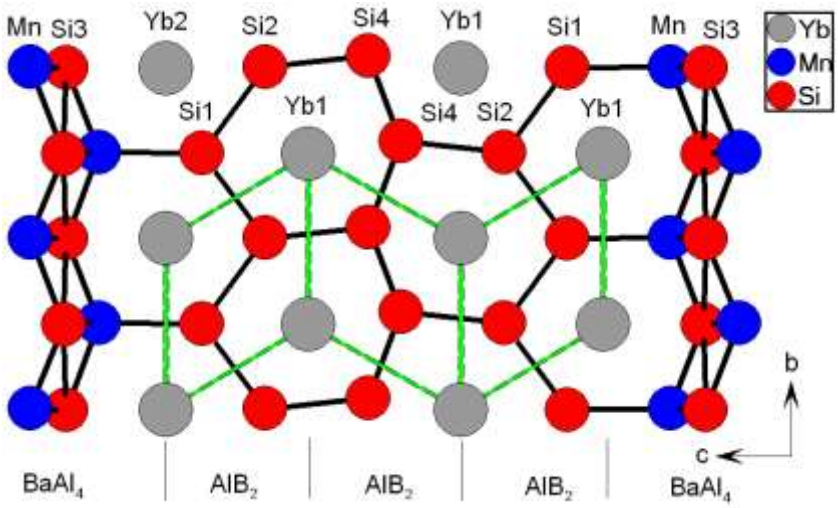

Figure 2. $BaAl_4$ and AlB_2 slabs in the crystal structure of $YbMn_{0.17}Si_{1.88}$. The unit cell of three AlB_2 layers are marked with solid green lines.

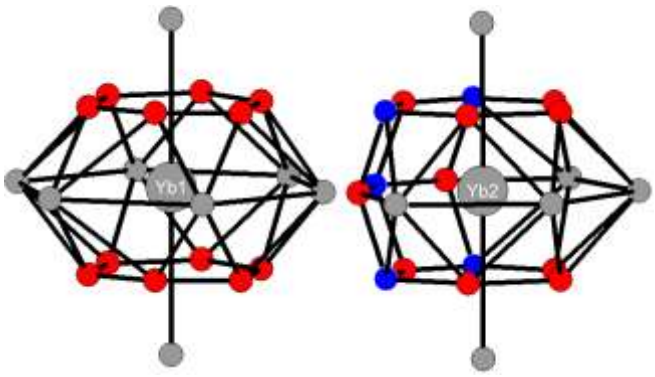

Figure 3. The cage like nearest neighbor environments of the two Yb positions in $YbMn_{0.17}Si_{1.88}$.

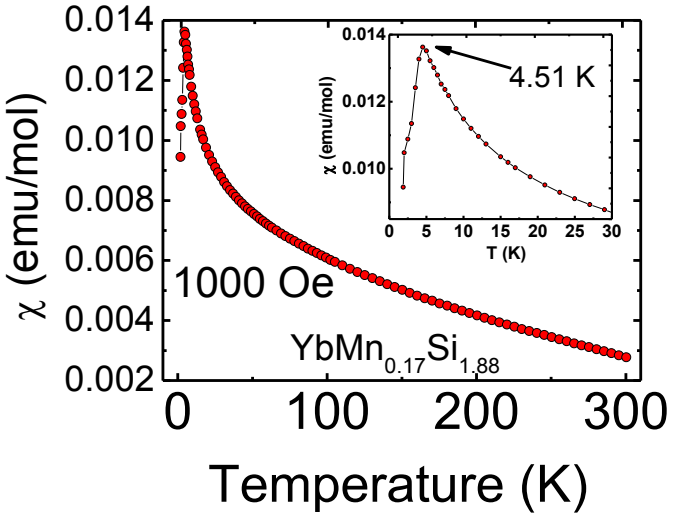

Figure 4. Magnetic susceptibility (χ = M/H) as a function of temperature for $YbMn_{0.17}Si_{1.88}$ (polycrystalline) sample measured in a dc field of 1 kOe. The inset figure shows magnetic ordering at ~5 K.

Magnetism

The temperature dependent magnetic susceptibility of $YbMn_{0.17}Si_{1.88}$ at an applied field of 1 kOe and the inverse molar magnetic susceptibility $1/\chi_m(T)$ data versus the temperature are shown in Figures 4 and 5, respectively. Above 40 K $YbMn_{0.17}Si_{1.88}$ exhibits paramagnetic behavior following Curie–Weiss law $\chi_m(T) = C/(T - \theta_p)$, where $C = N_A \mu_{eff}^2/3k_B = \mu_{eff}^2/8$ is the Curie constant and θ_p is the Weiss temperature. Linear least-squares fit of the data to this equation within the linear region of 50-200 K gives an effective moment μ_{eff} of 3.32 μ_B per formula and θ_p of -136 K. In general, the negative θ_p corresponds to predominant antiferromagnetic interactions in the compound. Above 200 K a slight deviation from linearity is observed and the calculated magnetic moment in the range 200-300 K is ~2.60 μ_B/Yb (57 % of Yb^{3+}) may be indicating a valence change occurring at ~200 K. A detailed temperature dependent X-ray absorption near edge spectroscopy is required to further confirm this speculation. Below 40 K the $\chi_m(T)$ data do not obey CW law and below 4.51 K the compound orders antiferromagnetically.

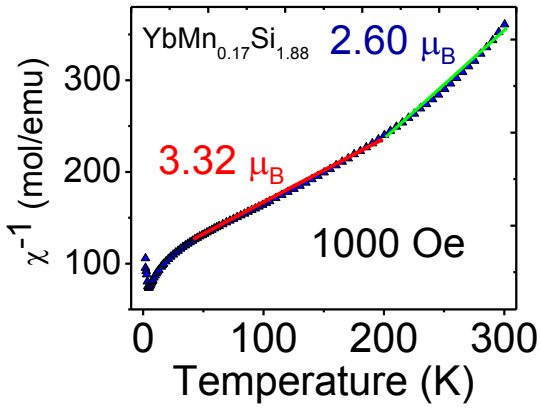

Figure 5. Inverse magnetic susceptibility (χ^{-1} = H/M) for polycrystalline sample of $YbMn_{0.17}Si_{1.88}$. The linear regions are marked with red and green sold lines.

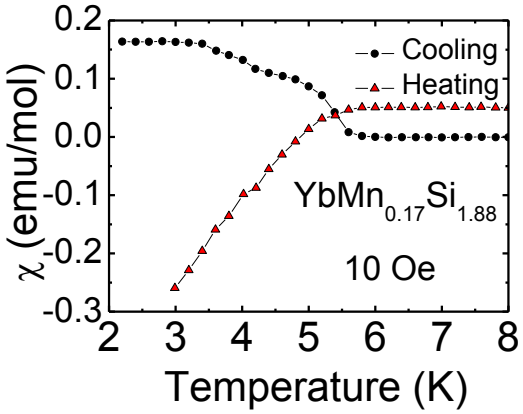

Figure 6. Temperature dependent susceptibility for $YbMn_{0.17}Si_{1.88}$ obtained on cooling and warming under 10 Oe.

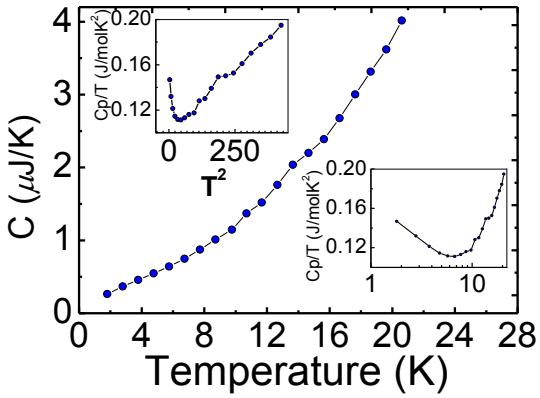

Figure 7. Heat capacity C_p for $YbMn_{0.17}Si_{1.88}$ measured as a function of temperature (T) at zero applied field. The inset figures show C_p/T vs. T and C_p/T vs. T^2.

Field dependent magnetic susceptibility measurements performed on $YbMn_{0.17}Si_{1.88}$ within the temperature range 2-300 K show that at low applied magnetic field 10 and 50 Oe a sudden negative magnetization was observed at 4.5 K, which we initially speculated to be a superconducting transition either from the compound or from adventitious indium in the samples. Indium is superconducting at 3.5 K

and this is reflected in the magnetic susceptibility measurements at lowest field possible (10 Oe). This difference clearly confirms that the negative magnetization of $YbMn_{0.17}Si_{1.88}$ is not from adventitious indium but from the compound. Electrical resistivity measurements show that there is no drop in resistivity around 4.5 K. Instead at 3 K the resistivity drop about 3% indicating traces of indium flux in the crystals of $YbMn_{0.17}Si_{1.88}$. Magnetization measurements of $YbMn_{0.17}Si_{1.88}$ carried at various temperatures starting from 2 K show as the temperature is raised to well above the ordering temperature (10 K) a smooth curve is obtained over the complete range of applied field which continues to higher temperatures.

Specific heat

Figure 7 shows the specific heat of $YbMn_{0.17}Si_{1.88}$ within the temperature range 2 -50 K with zero applied field. The inset figures shown are (a) C/T vs. T and (b) C/T vs. T^2. Within the Debye low temperature approximation the measured specific heat is given as:

$$C = \gamma T + \beta T^3 \text{ or } C/T = \gamma + \beta T^2 \qquad (1)$$

where γ is the contribution from the conduction electrons and β is the lattice contribution. The value of γ is proportional to the density of states near the Fermi energy. A fit to the experimental points resulted in a Debye temperature Θ_D of about 115 K, and an electronic specific heat coefficient $\gamma \approx 170$ mJ/mol K^2, which was determined from $\gamma (= C_p \text{ vs. } T)_{T \to 0}$ at low temperatures. Therefore, the compound may be a moderate heavy-fermion material according to the arbitrary classification of these systems into "light", "moderate" and classical heavy-fermions with γ values lying in the range of ~ 50-100, 100-400 and > 400 mJ / mol K^2, respectively.

Temperature dependent specific heat shows a smooth curve from 2 to 300 K, but both C/T vs. T and (b) C/T vs. T^2 shows anomalies (10 and 13 K in C/T vs T) which highlight the magnetic instabilities in this compound. The upturn in C/T vs. T and (b) C/T vs. T^2 observed at low temperatures is characteristic of many heavy fermion and moderate heavy fermion compounds.[4] In order to study the influence of the magnetic field on the specific heat further field dependent measurements will be needed. The semi-log plot in the inset of Figure 7 emphasizes the logarithmic increase of the electronic specific heat coefficient below 6 K in zero magnetic field. This type of dependence in the low-temperature part of $C(T)/T$ plot is reminiscent of non-Fermi-liquid (NFL) behavior, which may from the presence of the magnetic phase transition at low temperature.

References

1. Peter, S. C.; Chondroudi, M.; Malliakas, C. D.; Balasubramanian, M.; Kanatzidis, M. G. *J Am Chem Soc* **2011**, *133*, 13840.
2. Norlidah, N. M.; Ijjaali, I.; Venturini, G.; Malaman, B. *J. Alloys Compd* **1998**, *278*, 246.
3. Jutzi, P.; Schubert, U. Siilicon Chemistry, Wiley VCH, Weinheim, **2007**.
4. Falkowski, M.; Kowalczyk, A.; Tolinski, T. *Journal of Alloys and Compounds* **2011**, *509*, 6135.

Table 1. Crystal data and structure refinement for $YbMn_{0.17}Si_{1.88}$ at 293(2) K.

Wavelength	0.71073 Å
Crystal system	Monoclinic
Space group	$P2_1$
Unit cell dimensions	a = 4.0107(8) Å, α = 90.00° b = 3.8380(8) Å, β = 97.97(3)° c = 14.458(3) Å, γ = 90.00°
Volume	220.40(8) $Å^3$

Z	1
Density (calculated)	7.088 g/cm^3
Absorption coefficient	43.902 mm^{-1}
F(000)	402
Crystal size	0.10 x 0.08 x 0.08 mm^3
θ range for data collection	2.85 to 29.10°
Index ranges	-5<=h<=5, -5<=k<=5, -19<=l<=19
Reflections collected	2115
Independent reflections	1188 [R_{int} = 0.0408]
Completeness to θ = 29.10°	99.3%
Refinement method	Full-matrix least-squares on F^2
Data / restraints / parameters	1188 / 1 / 68
Goodness-of-fit	1.143
Final R indices [>2σ(I)]	R_{obs} = 0.0296, wR_{obs} = 0.0720
R indices [all data]	R_{all} = 0.0337, wR_{all} = 0.0742
Extinction coefficient	0.0047(7)
Largest diff. peak and hole	2.320 and -3.053 e·Å^{-3}

$R = \Sigma||F_o|-|F_c|| / \Sigma|F_o|$, $wR = \{\Sigma[w(|F_o|^2 - |F_c|^2)^2] / \Sigma[w(|F_o|^4)]\}^{1/2}$ and calc $w=1/[\sigma^2(Fo^2)+(0.0449P)^2+1.3738P]$ where $P=(Fo^2+2Fc^2)/3$

5) Personnel Participating in Project

Graduate students:
Melanie Francisco (PhD 2011)
Maria Chondroudi (PhD 2012)
Nickolas Calta, (5^{th} year graduate student, expected to get PhD end of 2015)

Postodocs:
Sebastian Peter, postdoctoral associate (50% support)

In 2011 Sebastian Peter has accepted an Assistant Professor position in Indian Institute of Technology (IIT) Bangalore, India and has been tenured in 2014.
A first graduate student is planned to be recruited for this project this fall. If this is not successful a postdoctoral fellow will be recruited.

Publications acknowledging financial support from this grant

(1) Francisco, M. C.; Malliakas, C. D.; Piccoli, P. M. B.; Gutmann, M. J.; Schultz, A. J.; Kanatzidis, M. G. Development and Loss of Ferromagnetism Controlled by the Interplay of Ge Concentration and Mn Vacancies in Structurally Modulated Y4Mn1-xGa12-yGey, *Journal of the American Chemical Society* **2010**, *132*, 8998-9006.

(2) Latturner, S. E.; Bilc, D.; Mahanti, S. D.; Kanatzidis, M. G. R3Au6+xAl26T (R = Ca, Sr, Eu, Yb; T = Early Transition Metal): a Large Family of Compounds with a Stuffed BaHg11 Structure Type Grown from Aluminum Flux, *Inorganic Chemistry* **2009**, *48*, 1346-1355.

(3) Macaluso, R. T.; Francisco, M.; Young, D. P.; Stadler, S.; Mitchell, J. F.; Geiser, U.; Hong, H. Y.; Kanatzidis, M. G. Structure and properties of rhombohedral CePd3Ga8: A variant of the cubic parent compound with BaHg11 structure type, *Journal of Solid State Chemistry* **2011**, *184*, 3185-3189.

(4) Peter, S. C.; Chondroudi, M.; Malliakas, C. D.; Balasubramanian, M.; Kanatzidis, M. G. Anomalous Thermal Expansion in the Square-Net Compounds RE4TGe8 (RE = Yb, Gd; T = Cr-Ni, Ag), *Journal of the American Chemical Society* **2011**, *133*, 13840-13843.

(5) Peter, S. C.; Kanatzidis, M. G. ThSi2 Type Ytterbium Disilicide and its Analogues YbTxSi2-x (T = Cr, Fe, Co), *Zeitschrift Fur Anorganische Und Allgemeine Chemie* **2012**, *638*, 287-293.

(6) Peter, S. C.; Rayaprol, S.; Francisco, M. C.; Kanatzidis, M. G. Crystal Structure and Properties of Yb5Ni4Ge10, *European Journal of Inorganic Chemistry* **2011**, 3963-3968.

(7) Sebastian, C. P.; Kanatzidis, M. G. The new binary intermetallic YbGe2.83, *Journal of Solid State Chemistry* **2010**, *183*, 2077-2081.

(8) Sebastian, C. P.; Kanatzidis, M. G. Ferromagnetic ordering in ThSi2 type CeAu0.28Ge1.72, *Journal of Solid State Chemistry* **2010**, *183*, 878-882.

(9) Sebastian, C. P.; Malliakas, C. D.; Chondroudi, M.; Schellenberg, I.; Rayaprol, S.; Hoffmann, R. D.; Pottgen, R.; Kanatzidis, M. G. Indium Flux-Growth of Eu2AuGe3: A New Germanide with an AlB2 Superstructure, *Inorganic Chemistry* **2010**, *49*, 9574-9580.

(10) Sebastian, C. P.; Salvador, J.; Martin, J. B.; Kanatzidis, M. G. New Intermetallics YbAu2In4 and Yb2Au3In5, *Inorganic Chemistry* **2010**, *49*, 10468-10474.

(11) Sieve, B.; Gray, D. L.; Henning, R.; Bakas, T.; Schultz, A. J.; Kanatzidis, M. G. Al Flux Synthesis of the Oxidation-Resistant Quaternary Phase REFe4Al9Si6 (RE = Tb, Er), *Chemistry of Materials* **2008**, *20*, 6107-6115.

(12) Wu, X. N.; Francisco, M.; Rak, Z.; Bakas, T.; Mahanti, S. D.; Kanatzidis, M. G. Synthesis, magnetism and electronic structure of YbNi(2-x)Fe(x)Al(8) (x=0.91) isolated from Al flux, *Journal of Solid State Chemistry* **2008**, *181*, 3269-3277.

(13) Zhuravleva, M. A.; Kanatzidis, M. G. Polygallide RE2MGa9Ge2 (RE = Ce, Sm; M = Ni, Co) Phases Grown in Molten Gallium, *Inorganic Chemistry* **2008**, *47*, 9471-9477.

(14) Calta, N. P.; Kanatzidis, M. G. Quaternary Aluminum Silicides Grown in Al Flux: RE5Mn4Al23,Six (RE = Ho, Er, Yb) and Er44Mn55(AlSi)237, *Inorganic Chemistry* **2013**, *52*, 9931-9940

Collaborations

Arthur J. Freeman, unfunded collaborator, no support.

We collaborated with with Drs Ulrich Welp, Wai Kowk, Ray Osborn of Materials Science Division, Argonne National Laboratory, and Dr Arthus Schultz and Mali Subramanian of APS also at Argonne National Laboratory.

3) Presentations:

Colloquia in Universities

1) November 2009, "The metallic flux as a synthesis tool for intermetallics", Colloquium, Department of Chemistry, University of Wisconsin.

2) February 2010, "The metallic flux as a synthesis tool for intermetallics", Colloquium, Stanford University.

3) November 2010, "The metallic flux as a synthesis tool for intermetallics", Colloquium, University of Michigan.

4) January 2011, "The metallic flux as a synthesis tool for intermetallics", Colloquium, Department of Chemistry, University of Notre Dame.

5) September 2011: "Fun with metallic fluxes: a synthesis tool for intermetallics", Colloquium, Department of Chemistry, University of Iowa.

6) April 2012: "A new class of rare earth silicides and germanides", Colloquium, Department of Chemistry, University of Iowa.

7) December 2012: "A new class of rare earth silicides and germanides", Colloquium, Department of Chemistry, University of Wisconsin.

National Meetings

1) August 2009, American Chemical Society National Meeting "Materials discovery in intermetallics using liquid metals as solvents", Washington, D.C.

2) Solid State Gordon Conference, New London, NH, August 2010.

3) 2011 North American Solid State Chemistry Conference, June 1-4, 2011, McMaster University, Hamilton, Ontario, Canada, Structure and phase transformations of REPd3-xGa8-x (RE = La,Ce,Nd,Sm,Tm,Yb): new variants of the cubic BaHg11 structure Type, Melanie C. Francisco, Northwestern University